J. Fluid Mech. (1980), *vol.* 99, *part* 1, *pp.* 13–31
Printed in Great Britain

Decaying turbulence in neutral and stratified fluids

By T. D. DICKEY† AND G. L. MELLOR
Geophysical Fluid Dynamics Program, Princeton University, New Jersey 08540

(Received 20 November 1978 and in revised form 12 October 1979)

Decaying turbulence in neutral and stratified fluids has been studied experimentally for relatively high mesh Reynolds numbers and long time-histories. The neutral case indicates an initial period decay law, $q^2 \propto t^{-1}$, through non-dimensional time

$$W_0 t/M \simeq 800$$

which is considerably longer than previous measurements at the same mesh Reynolds number ($Re = 48\,260$). The stratified experiment resulted in a decay rate virtually identical to that of the neutral case through $W_0 t/M = 275$. However the decay rate sharply decreased after this time when the field of turbulence was replaced by internal gravity waves. A critical Richardson number marks the transition from the turbulence to an internal gravity wave domain.

1. Introduction

The present study consists of two experiments. Experiment I is devoted to the evolution of grid-generated turbulence in a neutral fluid, while experiment II is identical to experiment I but the fluid is linearly stratified.

Many experiments have been devoted to the time history of homogeneous, isotropic turbulence produced by a grid in uniform flow wind tunnels under neutral conditions. Batchelor (1953) has reviewed much of the early work concerning these experiments. The studies using wind tunnels have been limited to relatively short decay times with high mesh Reynolds numbers or to low Reynolds numbers with longer decay times owing to limitations of wind-tunnel length. The present experimental design has enabled a study of turbulence with a combination of a long decay history, $W_0 t/M \lesssim 1100$, where W_0 is the grid velocity, t is time and M is mesh size, and high mesh Reynolds number,

$$Re = W_0 M/\nu = 48\,260,$$

where ν is the kinematic viscosity of water. Values of W_0 and M remain the same for all experiments. The accuracy of the present velocity measurements is dictated by sample size rather than instrumental noise. Grid-generated turbulence has been studied previously by Pao (1973), Lange (1974) and Lin & Veenhuizen (1974) for stratified fluids with horizontal rather than the vertical towing of the present experiment. Their work will be summarized in the discussion section.

† Present Address: Institute for Marine and Coastal Studies and Department of Geological Sciences, University of Southern California, University Park, Los Angeles, California 90007.

0022–1120/80/4461–1220 $02.00

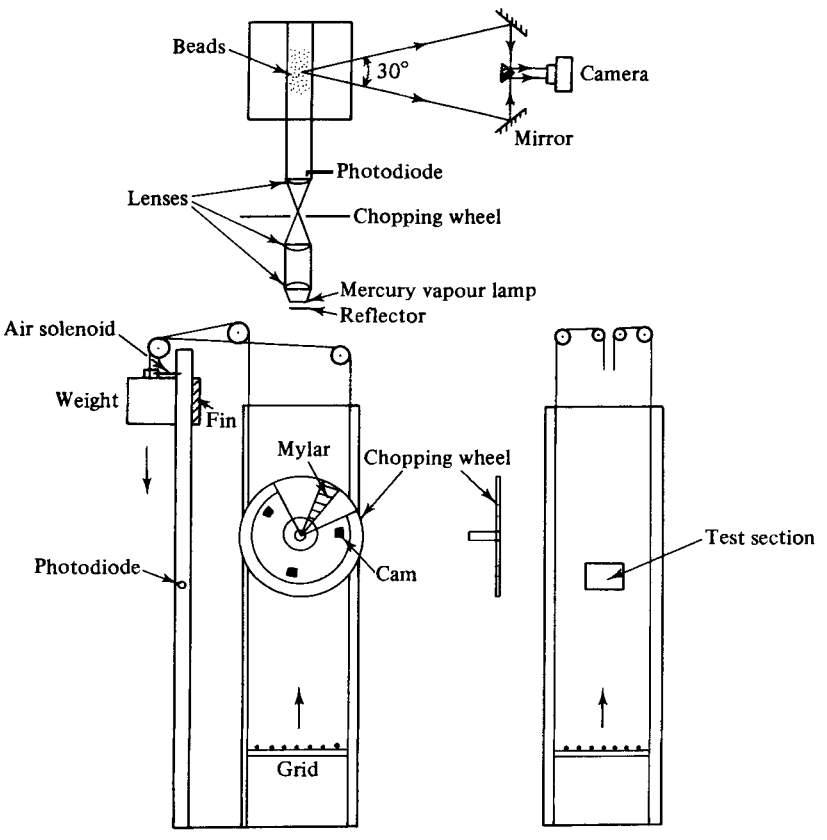

FIGURE 1. Schematic diagram of apparatus including experimental tank, grid towing mechanism, and photo-optical system. The dimensions of tank are 66 cm by 66 cm by 244 cm. The grid consists of 0·95 cm diameter rods with mesh size $M = 5{\cdot}08$ cm and solidity $\sigma_G = 0{\cdot}34$. The weight tows the grid. The mercury-vapour lamp illuminates the beads in test section. Plano-convex lenses (23 cm focal length) collimate light and light chopping-wheel controls exposure time. Light is reflected from the beads to the square mirrors, to the prism mirror, and then to the film plane of the camera.

2. Experimental technique

Turbulence was generated by a towed grid in a vertical tank in both neutral and stratified fluids as shown in figure 1. Trumbull (1967) designed the basic experimental set-up, and Falco (1971) converted the original photo-optical apparatus into a stereo system. A photodigitizing machine and a modified photographic streak geometry were employed in the present experiments.

The tank was constructed with two walls of aluminium sheet and two of plate glass. Marine plywood painted flat black provided the photographic background. The tank was filled or drained through a bottom port. The grid geometry and dimensions were the same as those used in many previous wind-tunnel experiments (e.g. Batchelor 1953). A release pin was activated to initiate the fall of a weight which towed the grid through the water column. A fin on the weight interrupted a light beam for a time interval measured with a photodiode, pulsed circuit, and an electronic timer; the accuracy was $\pm 0{\cdot}1$ ms. The grid velocity, W_g, was $95{\cdot}0 \pm 0{\cdot}4$ cm s^{-1} within $\pm 60{\cdot}0$ cm of the test section as determined from the fin interruption time and the fin length;

the mesh Reynolds number, $Re = W_0 M/\nu$, was 48260. The rotation of the light chopping wheel was initiated by the same photodiode. Neutrally buoyant beads of diameter $d = 0{\cdot}359 \pm 0{\cdot}062$ mm, which acted as tracers, were large enough for photographing yet small enough to follow all scales of motion. The distribution of densities of the beads was broad enough to permit their use in both neutral and stratified experiments.

Dark-field illumination of the tracer beads was obtained with a mercury-vapour lamp of brightness 40000 cd cm^{-2}. Low-quality lenses collimated the light giving a nearly cubic test section of side 12·7 cm. Light exposure was controlled by a light-chopping wheel with a semi-transparent material, Mylar, placed nearer one side of the slotted window. The resulting time-lapse photograph showed a short bright portion (head) and a long bright portion (tail) separated by a darker section; this provided a method of determining direction (figure 2*a*, plate 1). An exponentially decaying voltage was applied to the d.c. chopping-wheel motor which resulted in increasing exposure time and nearly constant tracelengths as the turbulence velocity decreased. The exposure time was determined with an accuracy of $\pm 0{\cdot}1$ ms by employing a photodiode near the chopping wheel, a pulsed circuit, and an electronic timer.

A 35 mm camera with motor drive, a 200 mm lens, and a relay box was used to photograph the tracer beads. The relay box was activated with each revolution of the chopping wheel, thus controlling the opening and closing of the shutter as well as advancing the film. The three components of velocity were determined from an image of each bead streak or trace as recorded on both left-hand and right-hand sides of the photograph (figure 2*a*). One of several reasons for using one camera was the necessity of recording common vertical co-ordinates of left and right images of each trace (i.e. left head matching vertical co-ordinates with right head). This was a requirement for the reconstruction of the three-dimensional velocity field.

Computation of the three components of velocity required a calibration of the system. A target board was composed of horizontal and vertical lines of known spacing and rods were mounted perpendicular to the plane of the board. It was placed in the experimental tank and photographed. The stereoscopic relations which convert the images of the bead trajectories to the three-dimensional velocity field are given in the appendix.

A photodigitizing machine, which was originally designed for high-accuracy measurements of track positions formed in bubble- or spark-chamber experiments, was utilized for measuring streaklengths of the tracer beads. Differences in alignment of the film were eliminated by use of fiducial points. Data obtained from the photodigitizing machine included calibration co-ordinates from the target photograph, fiducial-point co-ordinates and end points (heads and tails) for all traces. A computer program used this data and produced representations of the photographs (figure 2*b*).

The three-dimensional velocity field along with the location of each velocity vector was computed from the digitized data in the following manner. Target board and fiducial data were utilized to determine rotation angles for alignment of the co-ordinate system. Exposure times and calibration constants were also included as input parameters. Traces were sorted into left-hand and right-hand sides, and the vertical co-ordinates of the heads and tails of traces lying on each side were compared. Matching pairs were then determined using several geometric tests. In the process, almost half of the paired data was discarded. The three-dimensional velocities and positions of

the velocity vectors were computed using the stereoscopic relations along with the exposure times and stored on magnetic tape.

Since a time record of the turbulence energy was desired, photographs were taken with each revolution of the chopping wheel resulting in 19 frames per run. The elapsed times for all exposures were measured with an electronic timer. An adequate statistical sample was achieved after the experiment had been run 30 times. The velocities determined for each elapsed time were then ensemble averaged.

The same basic experimental arrangement prevailed for the experiment in a stratified fluid. A linear density profile $\partial\rho/\partial z = 1{\cdot}46 \times 10^{-4}\,(\mathrm{g\,cm^{-3}})\,\mathrm{cm^{-1}}$ was chosen for which the Brunt–Väisälä frequency N was 0·378 rad $\mathrm{s^{-1}}$. Conductivity measurements of local density were made in addition to velocity measurements. The method used in creating a linear density profile has been described by Fortuin (1960) and Orlanski (1972). A conductivity gauge, double-electrode conductivity probes, a digital voltmeter, and a chart recorder were used for the conductivity measurements. This system was described by Delisi & Orlanski (1975) and the conductivity probe technique has been reviewed by Maxworthy & Browand (1975). Samples of known densities were used to calibrate the output voltage of the conductivity gauge. Accuracy of conductivity measurements was approximately $\pm$ 1 %. Figure 3 illustrates a profile obtained with a traversing conductivity probe. The velocity measurement technique was identical to that of experiment I and tracelengths were optimized as before.

3. Data analysis

The velocity vectors were spatially and ensemble averaged over the test volume and all thirty runs for each time after passage of the grid for both experiments. The mean u component of such a sample for a given time was evaluated from

$$U = \frac{1}{N}\sum_{i=1}^{N} \tilde{u}_i, \tag{1}$$

where $\tilde{u}_i$ represented the instantaneous u component of velocity and N was the total number of events. The mean value of N was 680. The fluctuating component of the velocity was then given by

$$u_i = \tilde{u}_i - U. \tag{2}$$

The u component of twice the mean turbulence kinetic energy can be found by squaring u_i and ensemble averaging or

$$\overline{u^2} = \frac{1}{N}\sum_{i=1}^{N} u_i^2 = \overline{\tilde{u}^2} - U^2. \tag{3}$$

The other two components were computed similarly and the turbulence kinetic energy was given by

$$\tfrac{1}{2}q^2 = \tfrac{1}{2}(\overline{u^2} + \overline{v^2} + \overline{w^2}). \tag{4}$$

Two-point parallel turbulence velocity correlations were computed in the following way. The distance between a pair of turbulence velocity vectors was computed and the components of the vectors were resolved onto the connecting line. The product of the ith pair, $u_{p_i} u'_{p_i}$, along with all other pairs within the same photograph were

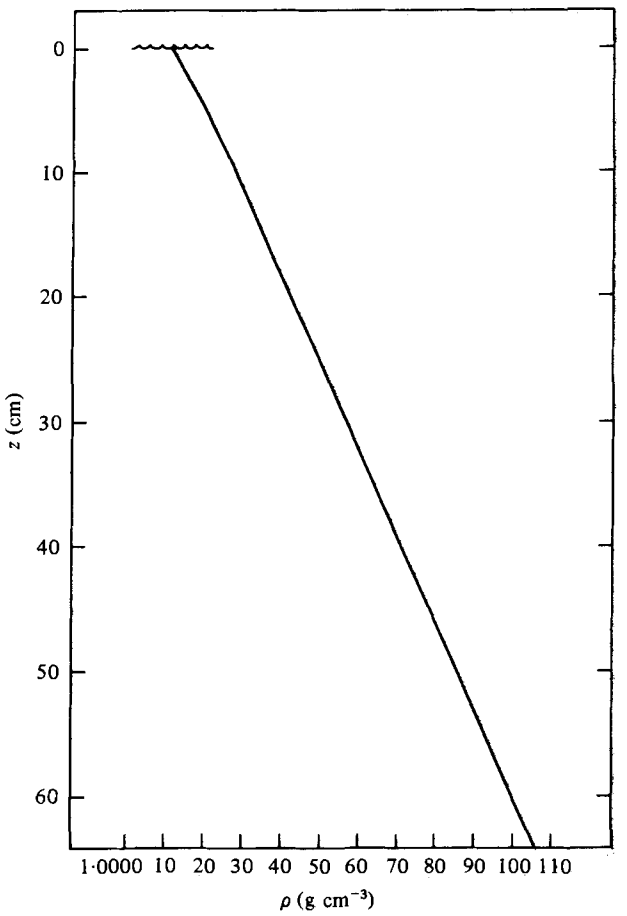

FIGURE 3. Depth verses density obtained with a traversing conductivity probe. Profile used for experiment II. $(\partial\rho/\partial z)_0 = 1{\cdot}46 \times 10^{-4}$ (g cm^{-3}) cm^{-1}.

found. All pairs with separation distances lying between $r-\frac{1}{2}\Delta r$ and $r+\frac{1}{2}\Delta r$ were averaged according to

$$\overline{u_p\, u_p'(r)} = \frac{1}{N_p}\sum_{i=1}^{N_p} u_{p_i}\, u_{p_i}'(r), \tag{5}$$

where N_p is the total number of pairs within an interval Δr and r is the mean separation distance. The interval Δr was chosen so that a statistically significant number of pairs would have separation distances in each interval. The upper limit of measured separation distances was established by the size of the test volume.

Errors in the values of velocity result from (1) the resolution of the photodigitizing system, (2) the calibration constants, and (3) the finite number of events. Error in the exposure time was negligible. Tracelengths measured by the photodigitizing system ranged from approximately 0·2 to 4·0 cm and the maximum percentage error was $\pm$ 0·5 %. The error due to uncertainty in values of the stereoscopic calibration constants was less than $\pm$ 0·1 %. The error due to finite sample size based upon the variances and correlation functions ranged from $\pm$ 5 to $\pm$ 12 %. An attractive feature of the present

technique is that the total percentage error can be further reduced by increasing sample size; instrument error is minimal.

4. Experimental results and their interpretation

We first discuss energy-decay data for turbulence in a neutral medium. Based on their laboratory experiments, Batchelor & Townsend (1948) defined an 'initial period' decay law whereby

$$\overline{w^2} \propto t^{-1}, \quad \lambda^2 \propto t; \tag{6}$$

λ was defined as a dissipation-length parameter (Taylor microscale). The turbulence Reynolds number, $Re_\lambda = (\overline{w^2})^{\frac{1}{2}}\lambda/\nu$, remains constant throughout the initial period. The final period decay law was determined on a theoretical basis such that

$$\overline{w^2} \propto t^{-\frac{5}{2}}, \quad \lambda^2 \propto t. \tag{7}$$

In the initial period the nonlinear inertial effects are important whereas in the final period they are not.

In the present data set for experiment I, the mean vertical velocity varied very nearly linearly from 0·49 cm s^{-1} at $W_g t/M = 107$ to 0·14 cm s^{-1} at $W_g t/M = 1111$. This small vertical mean flow was spatially constant in the test section and presumably was compensated by a return flow along the walls of the tank. The measured horizontal mean flows were negligible.

Within the error limits of the stereoscopic measurements, the transverse energy components, $\overline{u^2}$ and $\overline{v^2}$, were nearly isotropic. Therefore data (u and w components) were obtained from only one side of a photograph; since no matching criteria were applied, the sample size was approximately doubled and a reduction in error due to finite sample size resulted. (The full three-dimensional data set is used later for the correlation computations.) The components $\overline{u^2}$ and $\overline{w^2}$, as computed from the two-dimensional velocity data base, are shown in figures 4 and 5. These data indicate a linear relation between $1/\overline{u^2}$, $1/\overline{w^2}$ and $W_g t/M$ up to $W_g t/M \simeq 800$. A similar relation between $1/q^2$ and $W_g t/M$ is evident where $q^2 = 2\overline{u^2} + \overline{w^2}$ (figure 6). Thus, the initial period persists up to $W_g t/M \simeq 800$ for $Re = 48\,260$. The departure after this time is suggestive of transition to the final period.

Grid-generated turbulence generally results in a small degree of anisotropy. Batchelor (1953) suggested that the anisotropy results from the directional character of the grid and the method of generating the turbulence; efforts to limit anisotropy with wind-tunnel contractions have been pursued by several investigators including Uberoi (1956) and Comte-Bellot & Corrsin (1966). After $W_g t/M \simeq 100$, the present data show a nearly uniform value of $\overline{w^2}/\overline{u^2} = 1{\cdot}1$. Comte-Bellot & Corrsin (1966) and Schedvin, Stegen & Gibson (1974) also found trends toward isotropy with increasing time while their ratios of $\overline{w^2}/\overline{u^2}$ were also generally 1·1.

Since the present experimental method is somewhat unique, a comparison of our results with other experiments for shorter decay histories is warranted. The results of several experiments using comparable parameters for the range $W_g t/M < 120$ are shown in figure 7. All experiments indicate a near-linear dependence of $1/q^2$ on time with slightly different virtual origins and slope constants. The longitudinal data are plotted for those experiments which do not report q^2.

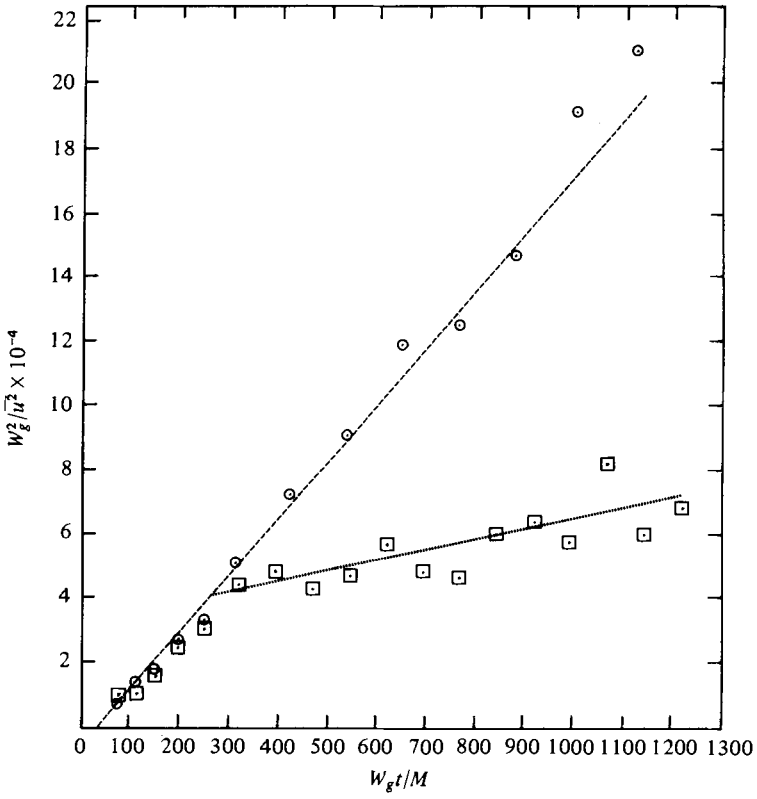

FIGURE 4. Decay of transverse component of turbulence kinetic energy for neutral and stratified cases. Two-dimensional data were used. Dashed lines are linear least-square fits to data. $W_g = 95{\cdot}0\,\mathrm{cm\,s^{-1}}$, $Re = 48\,260$, $M = 5{\cdot}08\,\mathrm{cm}$; ⊙, neutral; ⊡, $\partial\rho/\partial z = 1{\cdot}46 \times 10^{-4}\,(\mathrm{g\,cm^{-3}})\,\mathrm{cm^{-1}}$.

Results also have been cast into the standard empirical form

$$\frac{W_g^2}{\overline{u^2}} = A_x \left(\frac{W_g t}{M} - \frac{W_g t_0}{M}\right)^{n_x}, \tag{8}$$

where the subscript x denotes constants associated with the u component. Least-square fits of the data were used to evaluate the empirical constants. $W_g t_0/M$ is defined as the virtual origin and empirically represents the effect of the turbulence adjusting from a semi-organized state near the grid to a near-equilibrium, random field far from the grid. The quantity A_x is the slope constant and possibly relates to the grid geometry and Reynolds number; n_x is an empirical power constant. Constants A_T and n_T apply to twice the turbulence kinetic energy.

In table 1 the present data are compared with predecessor data obtained with hot-wire anemometers. The differences in the power n and the empirical constant A appear to arise at least in part from different methods of curve fitting. For example, the Uberoi & Wallis (1967) data can be described by $n_z = 1{\cdot}00$ and $A_z = 100$ or by $n_z = 1{\cdot}24$ and $A_z = 38$ and appropriate virtual origins.

Energy decay data from experiment II has been included in figures 4–6 for comparison with the neutral data. Before discussing these results, attention is directed to figure 8 which represents the mean velocity at each $W_g t/M$. The oscillation of the

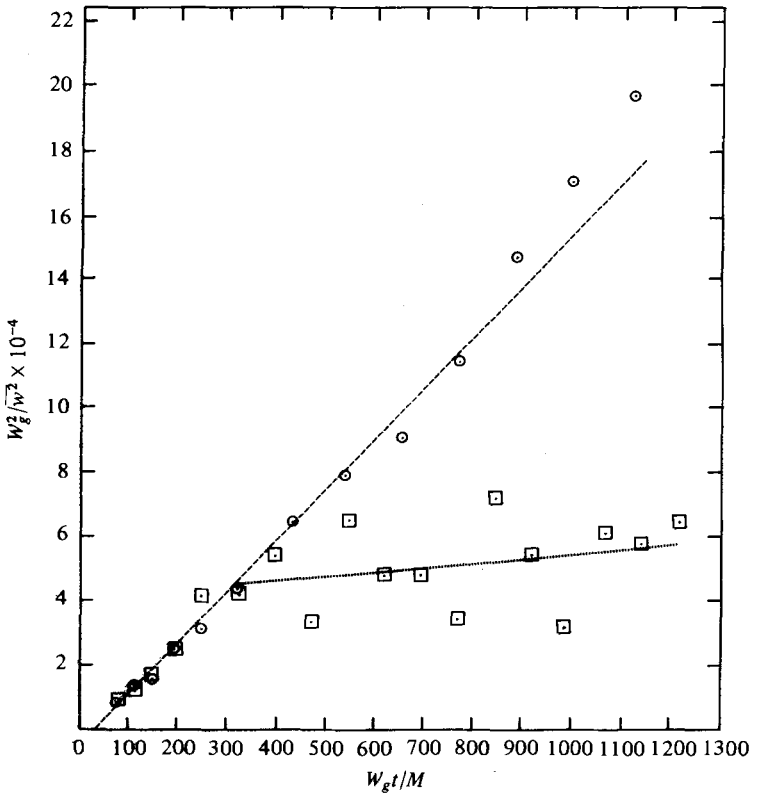

FIGURE 5. Decay of the longitudinal component of turbulence kinetic energy for neutral and stratified cases. Two-dimensional data were used. Dashed lines are the linear least-square fits to data. $W_g = 95{\cdot}0\,\mathrm{cm\,s^{-1}}$, $Re = 48260$, $M = 5{\cdot}08\,\mathrm{cm}$; ⊙, neutral; ⊡, $\partial\rho/\partial z = 1{\cdot}46 \times 10^{-4}\,(\mathrm{g\,cm^{-3}})\,\mathrm{cm^{-1}}$.

vertical component is very nearly equal to the Brunt–Väisälä frequency. From the internal gravity-wave dispersion relation we obtain

$$\sigma = N\left[\frac{k_x^2 + k_y^2}{k_x^2 + k_y^2 + k_z^2}\right]^{\frac{1}{2}}, \tag{9}$$

where σ is the frequency and (k_x, k_y, k_z) is the wavenumber vector. For $\sigma \simeq N$, we obtain $k_x \simeq k_y \gg k_z$. Thus, it seems reasonable to suppose that the mean velocity, W, in figure 8 is a manifestation of the gravest mode where the vertical and horizontal wavelengths are the tank height and widths respectively. This mode was very probably excited by the initial passage of the grid; its amplitude is nearly equal to the mean velocity of experiment I.

Figure 9 illustrates two time records of density resulting from conductivity-probe measurements. This technique was employed to give a qualitative account of the transition from turbulence to internal waves; in retrospect, more records should have been obtained to provide frequency spectra for the intervals $0 < W_g t/M < 300$ and $300 < W_g t/M < 1000$.

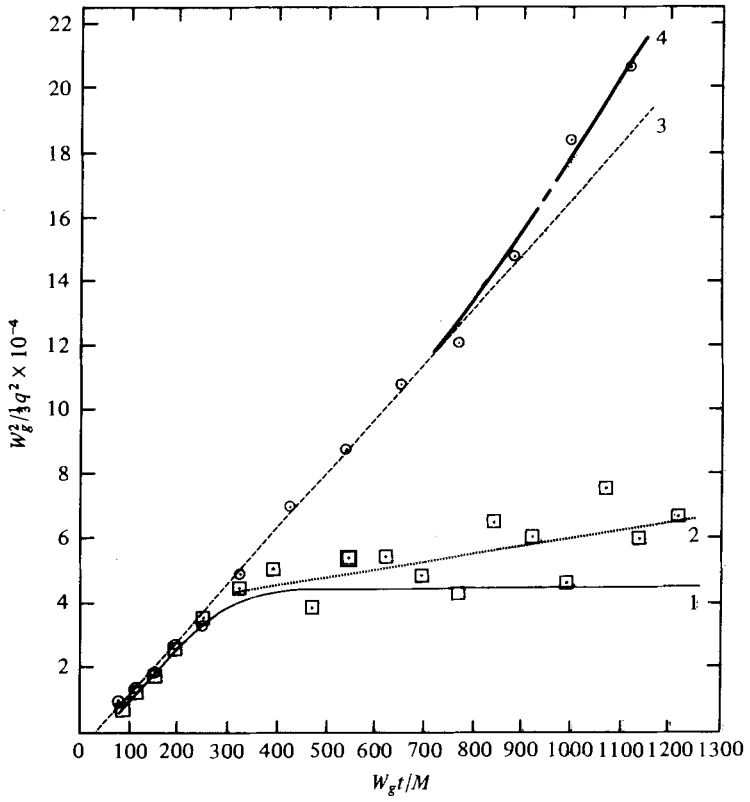

FIGURE 6. Decay of turbulence kinetic energy for neutral and stratified cases. Two-dimensional data were used. Curve 1 is the solution to equation (20); curve 2 is a linear least-square fit to data; curve 3 is the initial period decay law; and curve 4 is the solution to equations (13) and (14). $W_g = 95{\cdot}0\,\mathrm{cm\,s^{-1}}$, $Re = 48\,260$, $M = 5{\cdot}08\,\mathrm{cm}$; ⊙, neutral; ⊡, $\partial\rho/\partial z = 1{\cdot}46 \times 10^{-4}\,(\mathrm{g\,cm^{-3}})\,\mathrm{cm^{-1}}$.

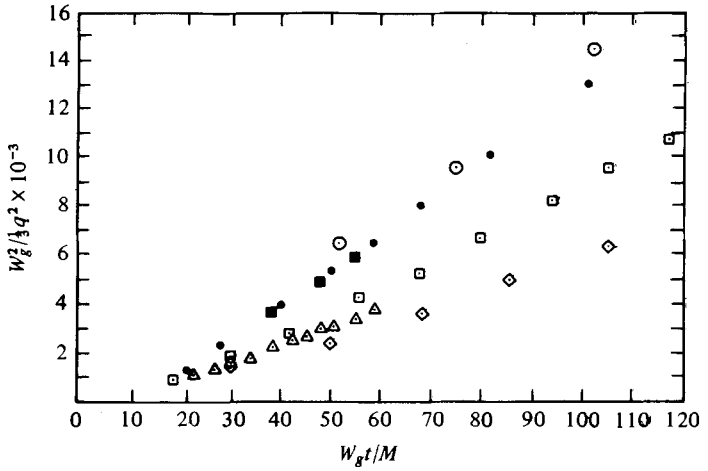

FIGURE 7. Comparison of decay of turbulence kinetic energy (neutral case) (see also table 1): ●, Batchelor & Townsend (1948), $Re = 11\,000$, $M = 1{\cdot}27\,\mathrm{cm}$; △, Kistler & Vrebalovich (1966), $Re = 2\,420\,000$, $M = 17{\cdot}1\,\mathrm{cm}$; ⊡, Uberoi & Wallis (1967), $Re = 51\,000$, $M = 5{\cdot}08\,\mathrm{cm}$; ◇, Comte-Bellot & Corrsin (1966), $Re = 34\,000$, $M = 2{\cdot}54\,\mathrm{cm}$; ■, Van Atta & Chen (1968), $Re = 25\,300$, $M = 5{\cdot}08\,\mathrm{cm}$; ⊙, present, $Re = 48\,260$, $M = 5{\cdot}08\,\mathrm{cm}$.

	Re $\times 10^{-3}$	M (cm)	σ_G	Rods	Medium	$\frac{W_g t}{M}$ range	n_x	n_z	n_T	A_x	A_z	$3A_T$	$\frac{W_g t_0}{M}$
Batchelor & Townsend (1948)	11·0	1·27	0·34	Rd.	Air	<200	—	1·00	—	—	151	—	15
Wyatt (1955)*	44·0	5·08	0·34	Rd.	Air	<100	—	1·25	—	—	35	—	0
Comte-Bellot & Corrsin (1966)	34·0	2·54	0·34	Sq.	Air	<400	1·24	1·27	—	23	18	—	2
Comte-Bellot & Corrsin (1966)	34·0	5·08	0·44	Rd.	Air	<200	1·24	1·30	—	37	23	—	2
Kistler & Vrebalovich* (1966)	2420	17·1	0·34	Rd.	Air	<60	1·00	1·00	—	110	71	—	0
Uberoi & Wallis (1967)	51·0	5·08	0·34	Rd.	Air	<120	1·24	1·24	—	51	37	—	17
Van Atta & Chen (1968)	25·3	5·08	0·34	Rd.	Air	<60	1·00	1·00	—	242	182	—	28
Gad-El-Hak & Corrsin (1974)	48·3	10·2	0·37	Rd.	Air	<90	1·33	1·32	—	16	13	—	0
Schedvin, Stegen & Gibson (1974)	408	22·9	0·30	Sq.	Air	<41	—	—	1·00	—	—	—	0
Present	48·3	5·08	0·34	Rd.	Water	<800	1·00	1·00	1·00	177	159	170	27

TABLE 1. Results of various neutral decaying turbulence experiments. Curve fits by Gad-El-Hak & Corrsin (1974) are indicated by asterisks.

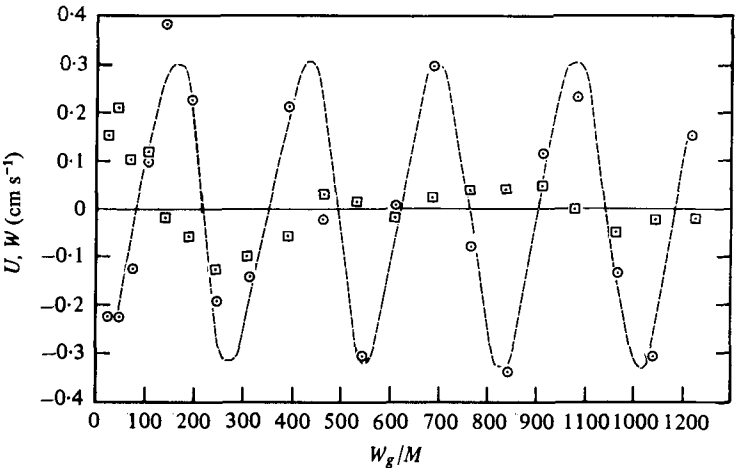

FIGURE 8. Transverse and longitudinal components of mean velocity as functions of non-dimensional time (experiment II). Dashed curve indicates a sinusoidal variation of W. Non-dimensional Brunt–Väisälä period $W_g \tau_{BV}/M = 310$. ⊙, W; ⊡, U.

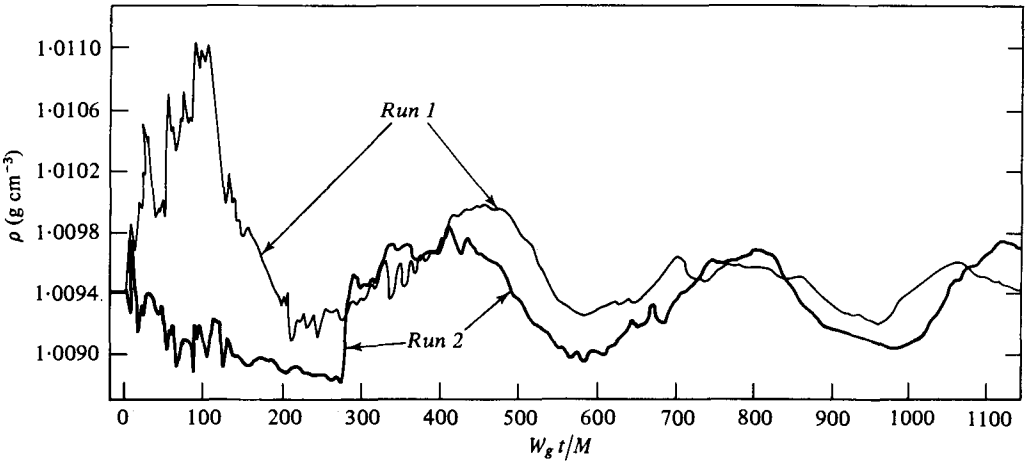

FIGURE 9. Density as a function of time for two runs obtained using conductivity probes (experiment II). Non-dimensional Brunt–Väisälä period $W_g \tau_{BV}/M = 310$. $W_g = 95{\cdot}0$ cm s^{-1}, $Re = 48\,260$.

The fluctuating energy components plotted in figures 4–6 exhibit a dramatic break in slope near $W_g t/M = 275$ representing an abrupt change from a turbulent regime, where, presumably, nonlinear inertial effects are important and buoyancy effects are not, to an internal wave regime where the reverse is true. Before the break the turbulence behaves as if it were neutral. After the break the behaviour is one of greatly reduced decay rate about which might appear to be a large amount of scatter. However, there is no identifiable cause for scatter in experiment II as compared with experiment I (or experiment II when $W_g t/M \lesssim 275$). Thus the variability of the data is real. A simple explanation is that the probability of the internal wave phase angle is not

uniformly distributed† since the turbulent creation of the internal wave field occurred in a span of time somewhat less than the Brunt–Väisälä period. There appears to be a discernible frequency in figure 6 of about $1{\cdot}3N$. Since the square of the internal wave amplitude is represented here, $\sigma \simeq 0{\cdot}65N$ is the internal wave frequency and from equation (9) $k_z/k_x = 1{\cdot}6$ presuming $k_x = k_y$. The decay rate from linear wave theory is $\nu k^2 q^2$, where $k^2 = k_x^2 + k_y^2 + k_z^2$. From the mean decay rate obtained from curve number 2 in figure 6 and if we assume all the waves are lumped at a single k, we thereby obtain $k \simeq 1\,\mathrm{cm}^{-1}$ or a wavelength of about 6 cm.

Two-point turbulence velocity correlations, $f(r) = \overline{u_p u_p'}/\overline{u_p^2}$, were averaged over three adjacent sample times in order to increase the number of events. The times given in figures 10–12 are thus the centre values. The number of events at small non-zero ($r \lesssim 3\,\mathrm{cm}$) and large ($r \gtrsim 10\,\mathrm{cm}$) separation distances results in greater error in correlations in those domains. The statistical sample was insufficient for triple correlations. Figures 10 and 11 (experiment I) indicate that energies of all scales are decaying proportionately within the accuracy of the measurement. The correlation data of Comte-Bellot & Corrsin (1971), who used $Re = 34000$ and $M = 5{\cdot}08$ cm for their wind-tunnel experiments, is in general agreement with our data (figure 10*a*).

It has been shown (Dickey & Mellor 1979) that the equation

$$\overline{uu'} - \overline{u^2} = F(\alpha)(\epsilon\nu)^{\frac{1}{2}} - 2\alpha\epsilon^{\frac{2}{3}}r^{\frac{2}{3}} \tag{10}$$

holds for small values of the correlation separation distance greater than about $10(\nu^3/\epsilon)^{\frac{1}{4}}$, where α is an empirical coefficient dependent upon Reynolds number and

$$F(\alpha) = 6{\cdot}96\alpha - 1{\cdot}41. \tag{11}$$

Equation (10) is plotted in figure 10 and is helpful in gauging the consistency of the data.

Correlations were computed for the stratified case (experiment II) in a fashion similar to that of experiment I and are shown in figures 10 and 12. They are similar to those of the neutral case up to $W_0 t/M = 246$; however, at later times they are greater than in the neutral case.

The integral length scale, L, is a rough measure of the distance within which velocities are correlated. The definition of L is

$$L = \int_0^\infty f(r)\,dr. \tag{12}$$

† For simplicity consider one velocity and frequency component, $u = A\sin(\sigma t + \phi)$, where A is amplitude, σ is frequency, and ϕ is phase angle. Then,

$$\overline{u^2} = \int\int u^2 P(A,\phi)\,dA\,d\phi.$$

Assuming the probability density, $P(A,\phi) = P(A)\,P(\phi)$, then

$$\overline{u^2} = (\overline{A^2}/2)\left[1 + \sin 2\sigma t \int_0^{2\pi} P(\phi)\sin 2\phi\,d\phi - \cos 2\sigma t \int_0^{2\pi} P(\phi)\cos 2\phi\,d\phi\right].$$

If $P(\phi) = \text{constant} = (2\pi)^{-1}$, the $\overline{u^2}$ signal contains no oscillations; otherwise there are oscillations with frequency 2σ.

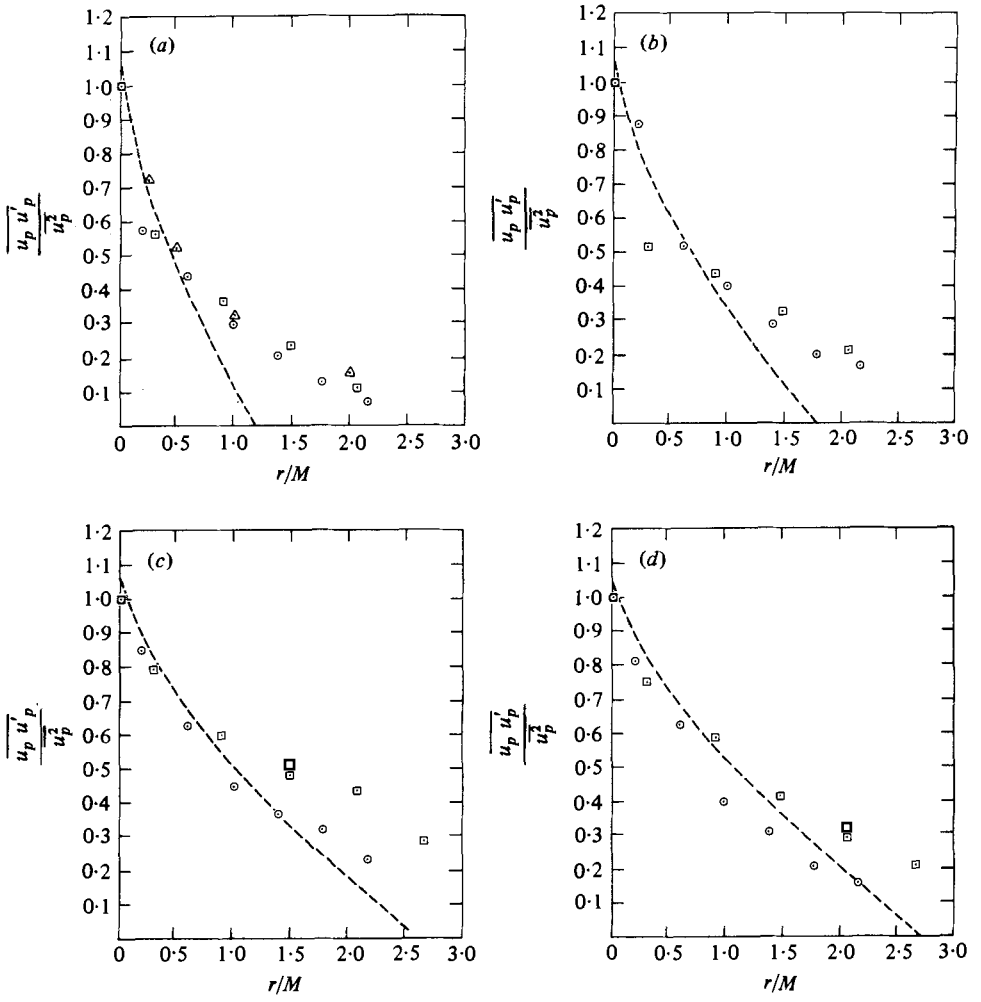

FIGURE 10. Normalized turbulence velocity correlations for experiments I and II as functions of non-dimensional separation distance. (*a*) ⊙, $W_g t/M = 189$, neutral; ⊡, $W_g t/M = 249$, stratified; △, $W_g t/M = 171$, neutral, Comte-Bellot & Corrsin (1971), $Re = 34000$, $M = 5{\cdot}08$ cm. (*b*) ⊙, $W_g t/M = 422$, neutral; ⊡, $W_g t/M = 468$, stratified. (*c*) ⊙, $W_g t/M = 764$, neutral; ⊡, $W_g t/M = 765$, stratified. (*d*) ⊙, $W_g t/M = 1111$, neutral; ⊡, $W_g t/M = 1137$, stratified. Dashed curves represent $f(r)$ determined from equation (10) and $\alpha = 0{\cdot}36$. A length scale for experiment I is indicated by the value of r at $f(r) = 0$.

The values of L^2 computed with the trapezoidal method are shown in figure 13. An inverse cube law† was used to extrapolate our data set for the region $r > 2{\cdot}0M$.

According to initial period arguments, L^2 should increase linearly with time in the

† The integral length scales were computed according to

$$L_n = L_\infty + \int_{r_0}^{\infty} f_0 \left(\frac{r_0}{r}\right)^n dr = L_\infty + \frac{f_0 r_0}{n-1},$$

where $r_0 \approx 2M$ and $f_0 = f(r_0)$. The real L is bounded by L_2 and L_∞ where in the neutral case L_2 is 20 % greater than L_∞. Therefore we have used an intermediate value, $L = L_3$, so that the error due to the extrapolation is ± 10 % or less.

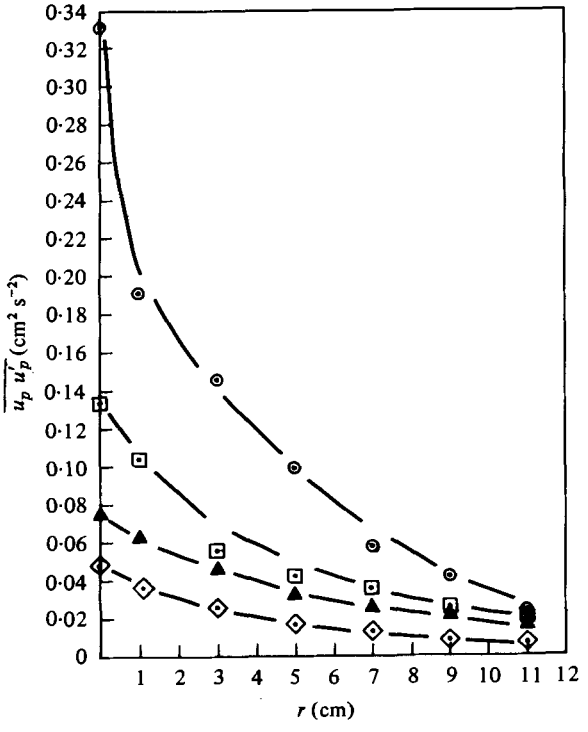

FIGURE 11. Turbulence velocity correlation as a function of separation distance (experiment I). $W_g = 95{\cdot}0\,\mathrm{cm\,s^{-1}}$, $Re = 48260$, $M = 5{\cdot}08$, neutral. $W_g t/M$ values: ⊙, 189; ⊡, 422; △, 764; ◇, 1111.

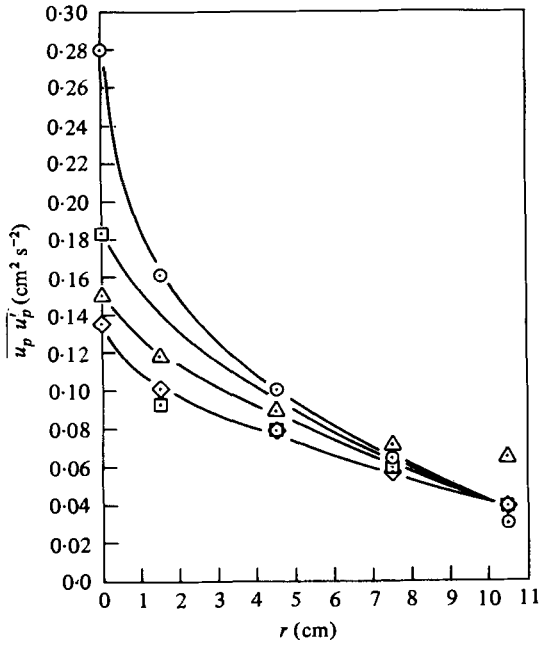

FIGURE 12. Turbulence velocity correlation as a function of separation distance (experiment II). $W_g = 95{\cdot}0\,\mathrm{cm\,s^{-1}}$, $Re = 48260$, $M = 5{\cdot}08$, $\partial\rho/\partial z = 1{\cdot}46 \times 10^{-4}$ (g cm^{-3}) cm^{-1}, stratified. $W_g t/M$ values: ⊙, 249; ⊡, 468; △, 765; ◇, 1137.

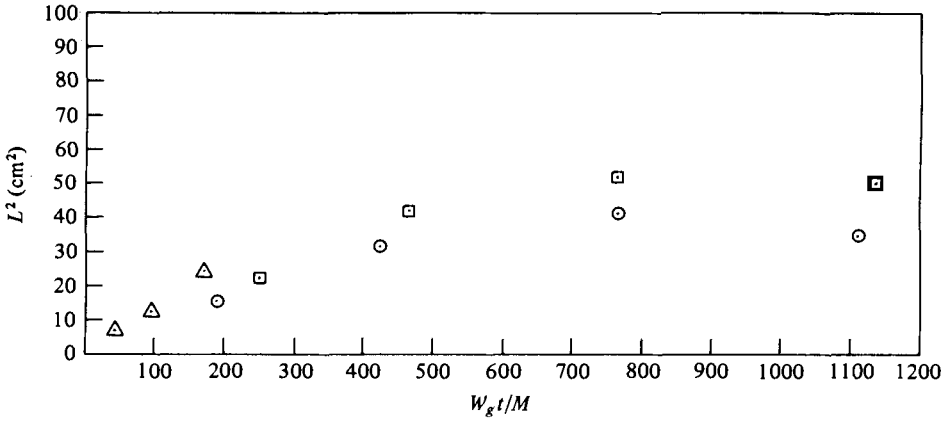

FIGURE 13. Integral length scale squared as a function of non-dimensional time (experiments I and II): ⊙, neutral; ⊡, stratified. The longitudinally determined integral length scales of Comte-Bellot & Corrsin (1971) are included (△) for their neutral experiment ($Re = 34000$ and $M = 5{\cdot}08$ cm).

neutral case. Our data indicate that the initial period is appropriate for $W_g t/M \lesssim 500$ on this basis. The integral length scales were also computed from the correlation function data for experiment II and are shown as functions of non-dimensional time in figure 13. An approximately linear relationship exists between L^2 and $W_g t/M$ up to $W_g t/M \approx 600$, remaining approximately constant thereafter.

5. A model of the energy decay for experiment I

By now a fairly standard model (Batchelor 1953) for dissipation is $\epsilon = q^3/\Lambda$, where Λ is a macro-scale. Thus, the turbulent kinetic equation is

$$\frac{d(\frac{1}{2}q^2)}{dt} = -\frac{q^3}{\Lambda}. \tag{13}$$

For $\Lambda \propto t^{\frac{1}{2}}$, as is observed for $W_g t/M \lesssim 500$ in figure 13, one obtains $q^2 \propto t^{-1}$ from (13), as is observed in figure 6 (neutral case) for $W_g t/M \lesssim 800$. The observed departure of q^2 from t^{-1} behaviour is seemingly too abrupt and does cast suspicion on the two data points for $W_g t/M > 900$ although there is no obvious reason why these data points are uniquely in error. The departure of Λ from $t^{\frac{1}{2}}$ behaviour is also curious. Let us, therefore, attempt to solve (13) by assuming $\Lambda(t) \propto L(t)$. In fact, from the initial period decay data of figure 6 and from figure 13 we can calculate that $\Lambda = (4{\cdot}6 \pm 0{\cdot}5)L$. Furthermore, from figure (13) a reasonable approximation for $\Lambda^2(t)$ is the ramp function,

$$\frac{\Lambda^2}{\Lambda_0^2} = \begin{cases} t/T, & 0 \leqslant t/T < 1, \\ 1, & 1 \leqslant t/T, \end{cases} \tag{14}$$

where Λ_0 and T are constants. Therefore, a solution to (13) and (14) is

$$\frac{\Lambda_0^2}{T^2}\frac{1}{q^2} = \begin{cases} 4t/T, & 0 \leqslant t/T < 1, \\ (1+t/T)^2, & 1 \leqslant t/T. \end{cases} \tag{15}$$

From figure 13 we estimate the transition from $\Lambda^2 \propto t$ to $\Lambda^2 = \Lambda_0^2$ to occur at

$$W_g t/M \simeq 600,$$

where $L^2 \simeq 40\,\text{cm}^2$. We therefore obtain $T = 600M/W_g$ and $\Lambda_0 = 33\,\text{cm}$, enabling us to plot equation (15) in figure 6 as curve number 4. Note that q^2 deviates very little from t^{-1} behaviour for a considerable time after the transition point. Then, the departure is fairly abrupt and faithfully replicates the data. Therefore, the model and data are self-consistent and, while not proof of simultaneous validity, it appears highly likely that the observed transition of $\Lambda(t)$ and $q^2(t)$ from initial period behaviour is real. One is further tempted to speculate that the transition is a precursor to final period decay described by equation (7).

6. A model of the energy budget for experiment II

The salient feature of experiment II was an abrupt decrease in dissipation. In order to understand this data we present, here, a very simple model which expresses the observed behaviour in terms of a simple dissipation hypothesis.

The dissipation-rate model for neutral flows, $\epsilon = q^3/\Lambda$, is inappropriate for the stratified case after $W_g t/M = 275$. The quantities pertinent to the flow include turbulence kinetic energy $\frac{1}{2}q^2$, a length scale Λ, and the Brunt–Väisälä frequency N. A non-dimensional quantity relevant to the onset of waves is $N\Lambda/q$. The simplest model of the dissipation rate is therefore

$$\epsilon = q^3/\Lambda - cN^3\Lambda^2, \tag{16}$$

where c is a constant to be determined empirically. The turbulence kinetic energy equation is then given by

$$\frac{d(\frac{1}{2}q^2)}{dt} = -\frac{q^3}{\Lambda}\left[1 - c\left(\frac{N\Lambda}{q}\right)^3\right] \tag{17}$$

since it was possible to determine from mean salt measurements that the buoyancy flux production term was negligible.

Since both q and Λ are functions of time, another equation is required to close the problem. A turbulence length-scale equation, which is a modified version of one proposed by Rotta (1951), has the form

$$\frac{d}{dt}(q^2\Lambda) = -q^3\left[1 - c\left(\frac{N\Lambda}{q}\right)^3\right]. \tag{18}$$

An empirical constant originally inserted into the right side of (18) has been adjusted so that (17) and (18) yield the initial period decay law for the neutral case, $N = 0$. By multiplying equation (17) by Λ and subtracting it from equation (18), it is found that

$$\frac{d}{dt}(q^2\Lambda^2) = 0, \tag{19}$$

or

$$q\Lambda = I = \text{constant}.$$

The length scale Λ can be eliminated from the turbulence kinetic-energy equation so that

$$\frac{d(\frac{1}{2}q^2)}{dt} = -\frac{q^4}{I} + c\frac{I^2N^3}{q^2}. \tag{20}$$

This equation can be separated and integrated, resulting in the solution

$$t = \frac{I}{2}\left\{\frac{1}{6\gamma}\ln\left[\frac{\gamma^2+\gamma q^2+q^4}{(\gamma-q^2)^2}\right] - \sqrt{\tfrac{1}{3}}\,\gamma^{-1}\tan^{-1}\left[\frac{2q^2+\gamma}{\sqrt{3}\,\gamma}\right]\right\} + t_0 + \frac{\pi I}{4\sqrt{3}\,\gamma}, \tag{21}$$

where $\gamma = c^{\frac{1}{3}}NI$ and the last two terms on the right are evaluated from the initial condition $q^{-2} = 0$ at $t = t_0$. Equation (21) is plotted in figure 6. The constant $c = 10^{-3}$ was determined from a fit to the data. An interpretation of c is obtained by considering (20) for large times when $dq^2/dt = 0$ and $q^6 = cI^3N^3$. A critical Richardson number, Ri_c, can therefore be defined and evaluated as

$$Ri_c = \left(\frac{N^2\Lambda^2}{q^2}\right)_c = c^{-\frac{2}{3}} = 100. \tag{22}$$

Another critical Richardson number, this one based upon the integral length scale, L, can be defined as

$$Ri_c' = \left(\frac{N^2L^2}{q^2}\right)_c = 4{\cdot}7 \tag{23}$$

since we had previously determined that $\Lambda = 4{\cdot}6L$. Finally, we note that the solution does not provide for viscous dissipation in the wave region as would be appropriate to high-Reynolds-number flow; this was purposeful in order to emphasize the abrupt decrease of ϵ which is directly related to the nonlinear cascade of energy-containing eddies.

7. Discussion

The decay of turbulence in salt-stratified fluids has been observed previously by Pao (1973), Lin & Veenhuizen (1974; see Lin & Pao 1979) and Lange (1974). These studies employed horizontally towed grids in stratified tanks. Pao (1973) observed the transition from turbulence to internal gravity waves using shadowgraphs; the internal wave period was near the Brunt–Väisälä period. Lin & Veenhuizen (1974) used hot-film and conductivity probes and shadowgraphs in their study. For a mesh Reynolds number of 45000 and an internal Froude number of 20 they found that decay rates of mean-square velocity fluctuations followed $t^{-\frac{4}{3}}$ and t^{-1} power laws for the horizontal components and a $t^{-\frac{2}{3}}$ law for the vertical component and for the decay of density variance. Thus, their velocity component decay rates differ from ours. Furthermore, there was no apparent transition from a turbulent regime to an internal wave regime as we have observed. Note, however, that we obtain transition at $W_g t/M \simeq 275$ for $W_g/(NM) \simeq 50$ whereas their experiment was restricted to $W_g t/M \simeq 100$ for $W_g/(NM) \simeq 20$; yet visual shadowgraphs suggest turbulence at $W_g t/M = 0$ and internal waves at $W_g t/M = 100$.

One might suppose that differences are related to the different experimental geometries, a vertical tank on the one hand and a horizontal channel on the other. However, we have been unable to devise a more detailed, scientific explanation.

Lange (1974) also measured salinity fluctuation statistics in a horizontal channel for a variety of flow parameters. It is difficult to relate data to specific parameters from the reference; however, his decay law for density variance is only crudely approximated by t^{-m}, where $0{\cdot}3 \lesssim m \lesssim 0{\cdot}6$; we can offer no reason why his results differ so much from those of Lin & Veenhuizen.

8. Conclusions

The results of the neutral decaying turbulence experiment indicate that the initial period decay law, $q^2 \propto t^{-1}$, for the relatively high mesh Reynolds number, 48260, prevails until $W_0 t/M \simeq 800$, after which a transition occurs. Previous measurements at comparable Reynolds numbers have been limited to the range $W_0 t/M \lesssim 400$. Anisotropy was small, $\overline{w^2}/\overline{u^2} \sim 1{\cdot}1$, throughout the experiment. Two-point parallel turbulence velocity correlation measurements were used in determining integral length scales, which were generally found to increase with the square root of time through $W_0 t/M \sim 500$, after which they remained approximately constant.

The effect of stratification upon a flow created by a vertically towed grid was investigated for the first time. Measurements indicated a turbulence-dominated regime through approximately $W_0 t/M = 275$, after which internal gravity waves were predominant. The decay rate of the turbulence was virtually the same as that of the neutral case through $W_0 t/M = 275$. However, after this time the decay rate was much lower. Integral length scales were computed as before with greater values being determined for the stratified case. A model for this experiment was developed wherein a critical Richardson number delineates turbulence and internal gravity wave regimes.

The present study was greatly facilitated by the previous work of Mr Hugh Trumbull, Dr Robert Falco, and Dr Tetsuji Yamada. The authors would like to thank Drs Alan Blumberg, Carmen Cerasoli, Frank Lipps, and Juergen Willebrand for their most helpful comments and suggestions. Laboratory support was provided by Mr Sam Goldman and Mr Gary Katona. The figures were illustrated by Mr William Ellis, Mr Philip Tunison, and Mr Michael Zadworney. The manuscript was typed by Mrs Toni Parker, Mrs Carol Bartlett, Mrs Jere Green, and Ms Rosalee Sierra. Primary support was provided by National Science Foundation grant ATM 75-19326; the Rosenstiel Research Fund of the University of Miami and the Institute for Marine and Coastal studies of the University of Southern California provided additional support.

Appendix. The stereoscopic relations

The equations relating positions of designated points (or heads and tails of traces) as recorded on the two sides of the film frame to the positions of the points in the test section of the tank are

$$\Delta X = C_x[(x_1' - x_2') + (x_1'' - x_2'')], \tag{A 1}$$

$$\Delta Y = C_y[(x_1' - x_2') - (x_1'' - x_2'')], \tag{A 2}$$

$$\Delta Z = C_z[(z_1' - z_2') + (z_1'' - z_2'')]; \tag{A 3}$$

ΔX, ΔY, and ΔZ represent component distances between designated points (or distances travelled by tracer beads) in the tank while x and z represent co-ordinates in the film plane. x is the horizontal component positive to the right, and z is the vertical component positive upward. A single prime represents left-image co-ordinates; double primes represent right-image co-ordinates; a subscript 1 represents designated point 1 or the position of the head of a trace; a subscript 2 represents designated point 2 or the tail of a trace. Knowledge of ΔX, ΔY, and ΔZ and all corresponding x's and

z's allowed the evaluation of C_x, C_y and C_z. The values were

$$C_x = 8{\cdot}98 \pm 0{\cdot}01, \quad C_y = 22{\cdot}74 \pm 0{\cdot}01 \quad \text{and} \quad C_z = 8{\cdot}89 \pm 0{\cdot}01.$$

REFERENCES

BATCHELOR, G. K. 1953 *The Theory of Homogeneous Turbulence*, p. 103. Cambridge University Press.

BATCHELOR, G. K. & TOWNSEND, A. A. 1948 Decay of isotropic turbulence in the initial period. *Proc. Roy. Soc.* A **193**, 539–566.

COMTE-BELLOT, G. & CORRSIN, S. 1966 The use of a contraction to improve the isotropy of grid-generated turbulence. *J. Fluid Mech.* **25**, 657–687.

COMTE-BELLOT, G. & CORRSIN, S. 1971 Simple Eulerian time correlation of full- and narrow-band velocity signals in grid-generated, 'isotropic' turbulence. *J. Fluid Mech.* **48**, 273–337.

DELISI, D. P. & ORLANSKI, I. 1975 On the role of density jumps in the reflexion and breaking of internal gravity waves. *J. Fluid Mech.* **69**, 445–464.

DICKEY, T. D. & MELLOR, G. L. 1979 The Kolmogorov $r^{\frac{4}{3}}$ law. *Phys. Fluids* **22**, 1029–1032.

FALCO, R. E. 1971 Measurements of the intensity and correlation from the initial period to the final period of decaying grid-generated turbulence. Ph.D. thesis, Princeton University.

FORTUIN, J. M. H. 1960 Theory and application of two supplementary methods of construction of density gradient columns. *J. Polymer Sci.* **44**, 505–515.

GAD-EL-HAK, M. & CORRSIN, S. 1974 Measurements of the nearly isotropic turbulence behind a uniform jet grid. *J. Fluid Mech.* **62**, 115–143.

KISTLER, A. L. & VREBALOVICH, T. 1966 Grid turbulence at large Reynolds numbers. *J. Fluid Mech.* **26**, 37–47.

LANGE, R. E. 1974 Decay of turbulence in stratified salt water. Ph.D. thesis, University of California, San Diego.

LIN, J. T. & PAO, Y. H. 1979 Wakes in stratified fluids. *Ann. Rev. Fluid Mech.* **11**, 317–338.

LIN, J. T. & VEENHUIZEN, S. D. 1974 Measurements of the decay of grid generated turbulence in a stably stratified fluid (abstract). *Bull. Am. Phys. Soc.* **19**, 1142–1143.

MAXWORTHY, T. & BROWAND, F. K. 1975 Experiments in rotating and stratified flows: Oceanographic application. *Ann. Rev. Fluid Mech.* **7**, 273–305.

ORLANSKI, I. 1972 On the breaking of standing internal gravity waves. *J. Fluid Mech.* **54**, 577–598.

PAO, Y. H. 1973 Measurements of internal waves and turbulence in two-dimensional stratified shear flows. *Boundary Layer Met.* **5**, 177–193.

ROTTA, J. C. 1951 Statistische Theorie nichthomogener Turbulenz. *Z. Phys.* **129**, 547–572, **131**, 51–77.

SCHEDVIN, J., STEGEN, G. & GIBSON, C. H. 1974 Universal similarity at high grid Reynolds numbers. *J. Fluid Mech.* **65**, 561–579.

TRUMBULL, H. 1967 A new research tool for the study of turbulent flows. M.S.E. thesis, Princeton University.

UBEROI, M. S. 1956 The effect of wind tunnel contraction on free stream turbulence. *J. Aero. Sci.* **23**, 754.

UBEROI, M. S. & WALLIS, S. 1967 Effect of grid geometry on turbulence decay. *J. Fluid Mech.* **10**, 1216–1224.

VAN ATTA, C. W. & CHEN, W. Y. 1968 Correlation measurements in grid turbulence using digital harmonic analysis. *J. Fluid Mech.* **34**, 497–515.

WYATT, L. A. 1955 Energy and spectra in decaying homogeneous turbulence. Ph.D. thesis, University of Manchester.

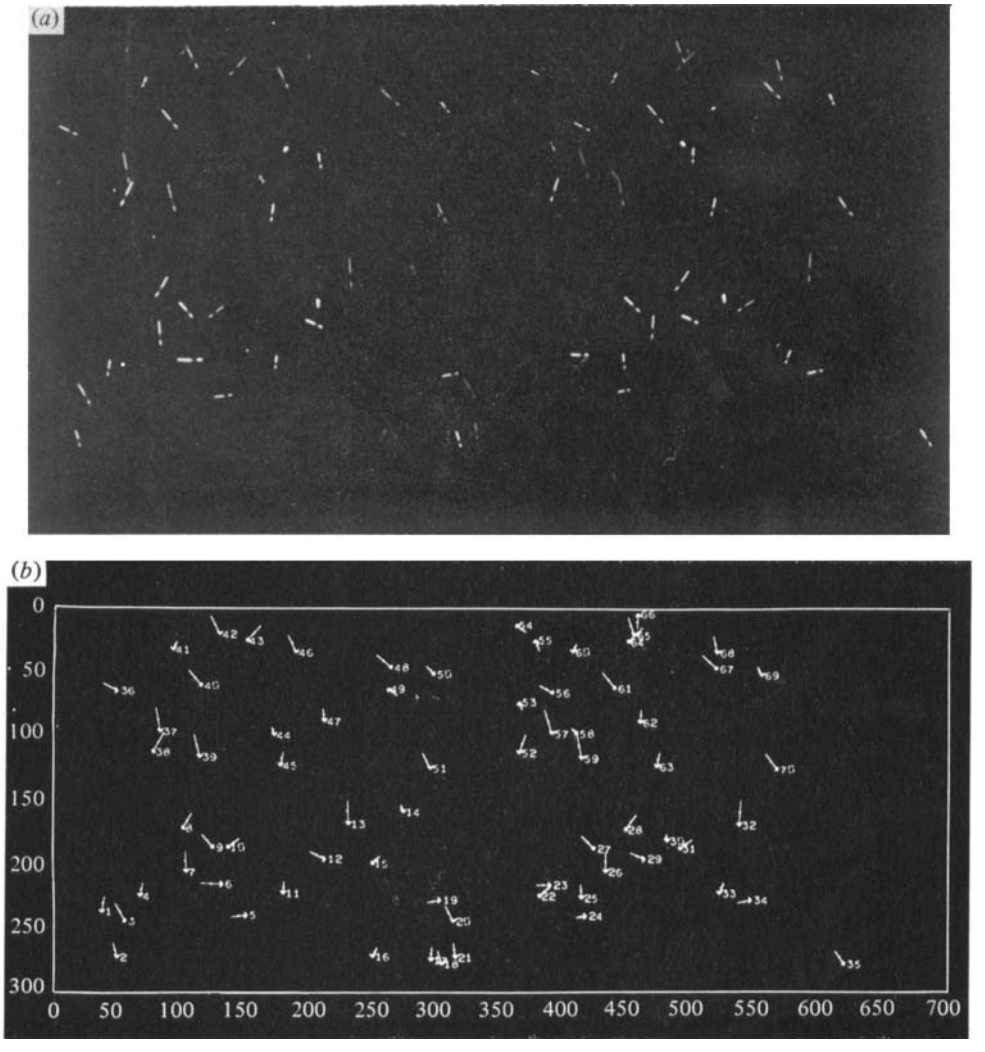

FIGURE 2. (*a*) An example of a streak photograph used for velocity determination. (*b*) Computer representation of streak photograph shown in (*a*). Note that the scales are not the same.